Structural basis for shieldin complex subunit 3–mediated recruitment of the checkpoint protein REV7 during DNA double-strand break repair

Yaxin Dai[‡§]**, Fan Zhang**[¶]**, Longge Wang**[‡§]**, Shan Shan**[‡]**, ⓘ Zihua Gong**[¶1]**, and ⓘ Zheng Zhou**[‡§2]

From the ‡*National Laboratory of Biomacromolecules, CAS Center for Excellence in Biomacromolecules, Institute of Biophysics, Chinese Academy of Sciences, Beijing 100101, China, the* §*Institute of Biophysics, University of Chinese Academy of Sciences, Beijing 100049, China, and the* ¶*Department of Cancer Biology, Cleveland Clinic Lerner Research Institute, Cleveland, Ohio 44195*

Edited by Patrick Sung

Shieldin complex subunit 3 (SHLD3) is the apical subunit of a recently-identified shieldin complex and plays a critical role in DNA double-strand break repair. To fulfill its function in DNA repair, SHLD3 interacts with the mitotic spindle assembly checkpoint protein REV7 homolog (REV7), but the details of this interaction remain obscure. Here, we present the crystal structures of REV7 in complex with SHLD3's REV7-binding domain (RBD) at 2.2–2.3 Å resolutions. The structures revealed that the ladle-shaped RBD in SHLD3 uses its N-terminal loop and C-terminal α-helix (αC-helix) in its interaction with REV7. The N-terminal loop exhibited a structure similar to those previously identified in other REV7-binding proteins, and the less-conserved αC-helix region adopted a distinct mode for binding REV7. *In vitro* and *in vivo* binding analyses revealed that the N-terminal loop and the αC-helix are both indispensable for high-affinity REV7 binding (with low-nanomolar affinity), underscoring the crucial role of SHLD3 αC-helix in protein binding. Moreover, binding kinetics analyses revealed that the REV7 "safety belt" region, which plays a role in binding other proteins, is essential for SHLD3–REV7 binding, as this region retards the dissociation of the RBD from the bound REV7. Together, the findings of our study reveal the molecular basis of the SHLD3–REV7 interaction and provide critical insights into how SHLD3 recognizes REV7.

DNA double-strand breaks (DSBs)[3] are extremely vicious DNA lesions that may cause carcinogenesis or cell death if not properly repaired. In vertebrate cells, two main repair pathways, nonhomologous end-joining (NHEJ) and homologous recombination (HR), are employed in eliminating the cytotoxic DSBs and thereby ensuring genomic integrity (1, 2). The decision-making process of repair pathways is a critical step during DSB response, which involves several elements such as the cell cycle state, the epigenetic regulation, and the DNA end resection (3, 4). 53BP1, in concert with its upstream regulators and downstream effectors, spearheads the restriction of end resection to promote NHEJ and antagonizes BRCA1-mediated HR repair, whose initiation step relies on resected DNA termini (5–14). Recently, several elegant studies have identified a previously-uncharacterized protein complex, named Shieldin, working as a downstream effector of 53BP1 to protect DNA end from resection and to facilitate NHEJ repair in a 53BP1-dependent manner (15–21). Similar to loss of 53BP1, deficient Shieldin leads to reactivation of end resection, impairs NHEJ activities, and affects the immunoglobulin class switching process (22).

Shieldin consists of four subunits: SHLD3 (also known as CTC-534A2.2 or RINN1); SHLD2 (also known as FAM35A or RINN2); SHLD1 (also known as C20ORF196 or RINN3); and REV7 (also known as MAD2L2). Apart from REV7, the other three Shieldin components had not been characterized before. Among these subunits, SHLD3 is the most apical element (16, 19, 22) that bridges REV7 to RIF1 and fills the gap in the 53BP1–RIF1–REV7 axis. Therefore, SHLD3 and REV7 form a sub-complex, which is considered as the DSB-recruitment module, while SHLD2, along with SHLD1, functions as the ssDNA-binding module within the complex (16). Knockdown of SHLD3 largely reduced the localization intensities of REV7/SHLD2/SHLD1 to the ionizing radiation-induced foci region, highlighting its RIF1-proximal role (16, 19). Importantly, depletion of SHLD3 dampens NHEJ-related events, activates DNA end resection, and restores HR in a BRCA1-mutated context, thus rendering these cells poly(ADP-ribose) polymerase inhibitors–resistant (15, 16, 19). Although SHLD3 is essential for recruitment and function of Shieldin by directly interacting with REV7, the underlying molecular mechanism remains elusive.

DNA; RBM, REV7-binding motif; IMAC, immobilized metal-affinity chromatography; Ni-NTA, nickel-nitrilotriacetic acid; IPTG, isopropyl β-D-thiogalactoside; TLS, translesion DNA synthesis; CAMP, chromosome alignment–maintaining phosphoprotein; SFB, S protein, FLAG, and streptavidin-binding peptide tag.

In this study, we report two crystal structures of REV7 in complex with the SHLD3–RBD. The complex structure shows that SHLD3–RBD forms a "ladle" configuration when it binds to REV7, comprising the N-terminal loop and the C-terminal α-helix (αC-helix) of SHLD3–RBD, which constitute the corresponding "stem" and "base" part of the ladle-shaped structure. The N-terminal loop is structurally similar to other REV7-binding proteins due to the presence of a well-established REV7-binding motif, but the αC-helix displays a binding mode distinct from known REV7-binding partners. Biochemical analyses, coupled with thermodynamic measurements, have verified their contribution to REV7 binding. Importantly, we demonstrated that the αC-helix region of SHLD3–RBD is a crucial contributing factor of robust SHLD3–REV7 interaction. Additionally, we present the first kinetic view on the "safety-belt" binding mechanism underlying the SHLD3–REV7 complex via surface plasmon resonance (SPR) assays. In sum, this work is the first structural study toward the role of REV7 in DSB repair and provides structural insights into how the DSB recruitment module assembles within the Shieldin complex.

Results

SHLD3 employs REV7-binding domain to interact with REV7

SHLD3 is a 250-amino acid polypeptide with a translational elongation initiation factor EIF4E-like domain in its C terminus (15) and contains two presumptive REV7-binding motifs (RBM, defined by P*XXX*pP sequence, where *X* represents any amino acid residue and the lowercase p is a less important proline residue and can be replaced by an alanine in some cases) in the N-terminal region (Fig. 1*a*). Previous work has mapped the region (residues 29–83), which harbors the second RBM in the N-terminal region of SHLD3 that interacts with REV7 (19). In agreement, we also observed this fragment (residues 29–83) displayed a tight binding to REV7 with a dissociation constant (K_D) of 13.8 ± 0.4 nM and a 1:1 binding stoichiometry (Fig. 1*b*), as measured by ITC assays. However, no binding was detected between the SHLD3 RBM1-containing peptide (residues 1–28) and REV7 (Fig. 1*b*), suggesting that the second RBM-containing region (residues 29–83) of SHLD3 plays a dominant role in dictating REV7 binding, although the first RBM may have other functions and is dispensable for this interaction. Multiple sequence alignment results also support this finding because the second RBM is invariably conserved in vertebrates, in stark contrast to the first RBM of poor conservation (Fig. S1*a*). We therefore generated the REV7–SHLD3(29–83) complex and performed crystallization trials. Analogous to previous reports, one (R124A) or two (R124A/A135D) dimer-breaking mutations were introduced into REV7 to improve protein homogeneity and promote crystal packing (23–25). But unfortunately, no crystals were obtained. Secondary structure prediction results suggested that the 29–60- and 74–83-amino acid regions of SHLD3 are mainly disordered (Fig. S1*a*), and the flexibility of these regions, we propose, may prejudice crystal packing. Hence, we next co-purified REV7 complexed with various truncated constructs of SHLD3 and found that the SHLD3(46–74) is sufficient for REV7 binding (Fig. S1*b*). Consistently, the SHLD3(46–83) peptide retained full binding

affinity as SHLD3(29–83) with a dissociation constant of 15.7 ± 0.8 nM in ITC measurement (Fig. 1*b*), indicating that the amino acid residues ranging from 29 to 45 of SHLD3, although conserved, are dispensable for REV7 interaction. Therefore, we named residues 46–74 of SHLD3 as the RBD and purified the REV7–SHLD3 (RBD) complex for the next round of crystal screening. Encouragingly, the REV7–SHLD3 (RBD) complex yielded diffraction-quality crystals.

Overall structure of the SHLD3–REV7 complex

The structures of the REV7[R124A]–SHLD3 (RBD) and REV7[R124A, A135D]–SHLD3 (RBD) complex were determined by the molecular replacement method using 2.2 and 2.3 Å resolution data, respectively. Both crystals contain one single copy of the SHLD3–REV7 complex per asymmetric unit, and residues 9–207 of REV7 and 49–73 of SHLD3 were successfully modeled, whereas other residues were not included in the final models due to indiscernible electron density. The crystallographic and geometric statistics of the refined models are exhibited in Table 1. Because these two structures are nearly identical, the REV7[R124A]–SHLD3 (RBD) structure with higher resolution was chosen as a representative for further description.

Within the structure, REV7 displays a canonical HORMA (<u>Ho</u>p1, <u>Rev</u>7, and <u>Mad</u>2) fold and adopts the closed conformation with SHLD3 peptide tightly held by the safety-belt loop of REV7 (Fig. 1*c*). Superimposition of REV7 in our complex with the previously reported structures of REV7/REV3–RBM1 (PDB code 3ABD) (24), REV7/CAMP (PDB code 5XPT) (26), and REV7/REV3–RBM2 (PDB code 6BC8) (25) revealed overall root mean square deviation (RMSD) values of 0.830, 0.953, and 0.915 Å, respectively, suggesting the global similarity of REV7 molecules in these protein complexes, except for some zones showing a high degree of flexibility (Fig. S2). The most striking difference occurs at the REV7 adaptor region (residues 156–174), which forms a short α-helix induced by SHLD3 binding (Fig. S2*a*), similar to the REV7 structure within the context of the TLS complex (Fig. S2*e*) (27–29) but distinct from the other reported REV7–RBM heterodimer complex where this region was either missing (24, 26) or subject to conformational changes (Fig. S2, *b–d*) (25). The structure diversity in this area reveals that the adaptor region of REV7 is capable of reorganizing its shape to accommodate various binding partners. Furthermore, the relative higher B factors of this region also reflect the structural flexibility and imply elasticity suitable for different binding sequences (Fig. S3).

Interestingly, SHLD3–RBD forms a ladle-shaped structure upon binding to REV7, with residues 49–58 (N-terminal loop region) and 59–73 (αC-helix region), respectively, constituting the "stem" and "base" of the ladle (Fig. 1*c*). The "stem" part contains a well-established RBM, and thus overlays well with other reported RBM, whereas the "base" region protrudes toward the back of REV7 and displays conformational variance compared with other REV7-binding peptides (see below).

Structural basis for REV7–SHLD3 interaction

The observed interaction between the N-terminal loop of SHLD3–RBD and REV7 is similar to other reported complexes due to the presence of RBM. In detail, residue Pro-50 of SHLD3
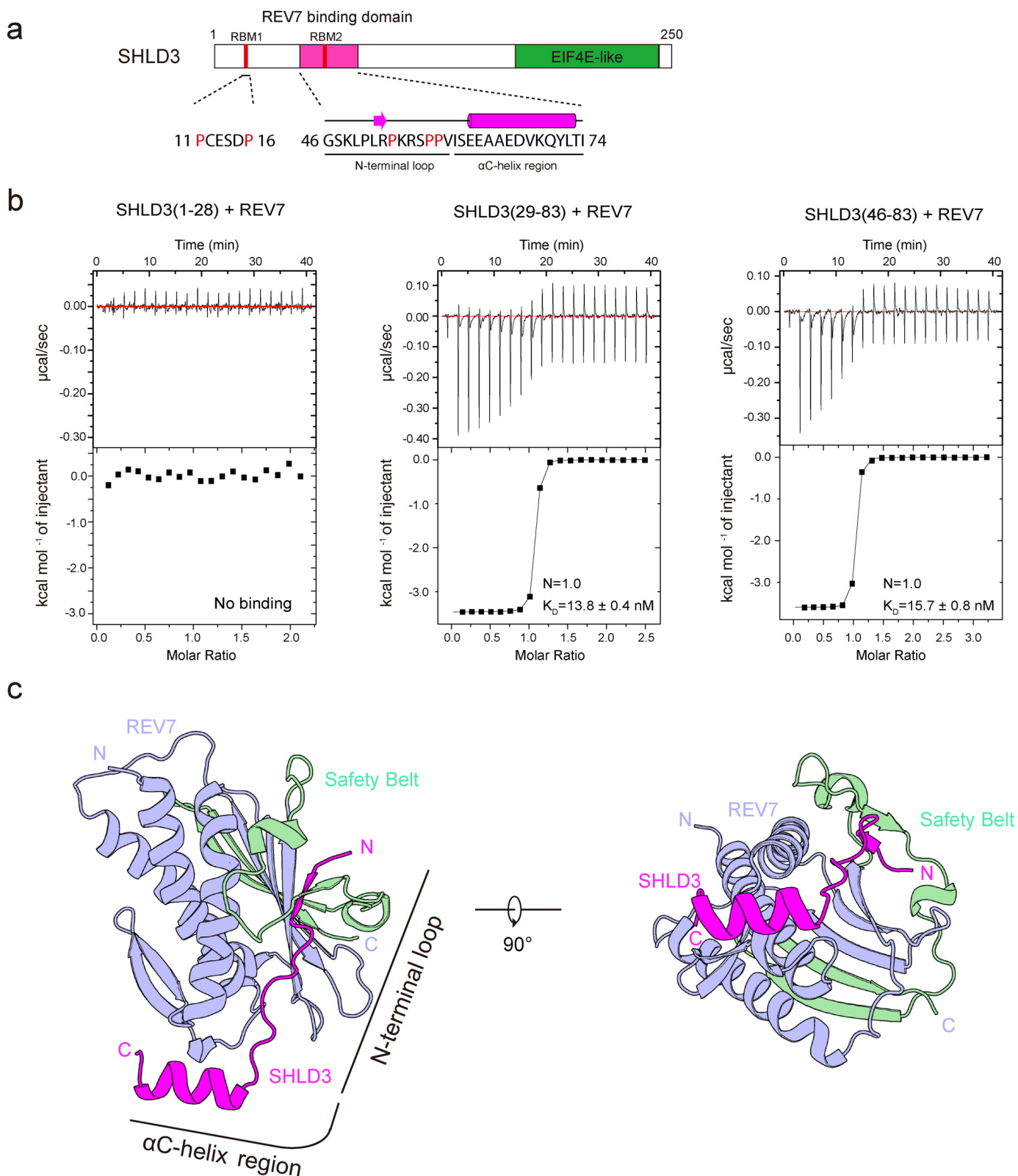
Figure 1. SHLD3 employs REV7-binding domain to interact with REV7. *a*, schematic domain architecture of SHLD3. The RBD and EIF4E-like domain of SHLD3 are depicted in *magenta* and *green,* respectively. The protein sequences of the presumptive REV7-binding motif 1 (RBM1) and RBD used in crystallization are displayed with the defined prolines in two RBMs colored in *red*. The secondary structure illustration of the RBD region is also shown *above* the protein sequence. *b*, isothermal titration calorimetric analysis of three different SHLD3 fragments binding to REV7. Raw data and fitting curves of the integrated data for various SHLD3 proteins are shown together with corresponding K_D values. *c*, overall structure of REV7 in complex of SHLD3 presented in *cartoon* mode. The SHLD3 fragment is shown in *magenta,* and the REV7 molecule is colored *light blue*, except for the C-terminal region of REV7, which is termed the safety-belt region (residues 153–207), highlighted in *pale green*. The N-terminal loop and αC-helix region of SHLD3–RBD are indicated.

Table 1
Data collection and refinement statistics
All diffraction data were obtained from a single crystal.

	SHLD3–REV7 (R124A)	SHLD3–REV7 (R124A/A135D)
Data collection		
Space group	P3$_2$21	P3$_2$21
Cell dimensions		
a, b, c (Å)	61.08, 61.08,133.24	60.64, 60.64, 133.48
α, β, γ (°)	90, 90, 120	90, 90, 120
Resolution (Å)	49.16–2.24 (2.31–2.24)[a]	44.49–2.31 (2.39–2.31)
R_{merge}	0.042 (1.019)	0.049 (0.935)
$I/\sigma I$	19.6 (2.4)	16.7 (2.4)
$CC_{1/2}$	0.999 (0.959)	0.999 (0.951)
Completeness (%)	99.8 (99.6)	99.9 (99.9)
Multiplicity	9.5 (10.1)	9.3 (9.8)
Refinement		
Resolution (Å)	49.16–2.24	44.49–2.31
Anisotropy (Å)[b]	2.5, 2.5, 2.2	2.6, 2.6, 2.3
No. of reflections	11,810	10,644
R_{work}/R_{free} (%)	20.4/24.6	21.0/26.2
No. of atoms		
Protein	1721	1728
Water	11	14
Ion/ligand	5	5
B-factors		
Protein	67.1	69.9
Water	59.6	57.8
Ion/ligand	126.2	153.0
RMSD		
Bond lengths (Å)	0.010	0.003
Bond angles (°)	1.059	0.626
Ramachandran plot		
Favored (%)	94.55	96.82
Allowed (%)	5.45	3.18
Outliers (%)	0	0
MolProbity score	1.74	1.43

[a] Values in parentheses are for the highest-resolution shell.
[b] Data were elliptically truncated along a*, b*, and c*, which indicate reciprocal cell directions, and reflections beyond these limits were excluded from refinement.

stacks its aliphatic ring with the aromatic side chain of His-151 of REV7 in a face–to–face manner, followed by residue Pro-53 wedging into a hydrophobic pocket formed by the aromatic side chains of Trp-171 and Phe-169 in REV7 (Fig. 2*a*). Both Pro-57 and Pro-58 of SHLD3 harmonize with another pocket in the REV7 surface where the phenyl ring of Tyr-63, along with Phe-146, clasps residue Pro-57 of SHLD3, and extensive van der Waal's interactions encircle residue Pro-58 of SHLD3 (Fig. 2*a*). Besides, these interactions are further stabilized by polar contacts formed by the hydroxyl groups of Tyr-63 and Tyr-37 side chains in REV7 with the backbone carbonyl oxygens from Arg-55 and Pro-58 of SHLD3 (Fig. 2*a*), respectively.

Regarding the αC-helix region, two residues, Ile-60 and Val-68 of SHLD3, are engaged in REV7 recognition. The side chains of Ile-60 and Val-68 fit well into a hydrophobic cavity formed by residues Tyr-37, Ile-41, and His-57 of REV7 (Fig. 2*a* and Fig. S4*a*), acting as two anchors. Additionally, the other residues in the α-helix also contribute to the complex formation through van der Waal's contacts with REV7.

N-terminal loop of SHLD3–RBD is required for REV7 interaction

To appraise the contribution of residues in the N-terminal loop to the SHLD3–REV7 interaction, we employed an *in vitro* co-purification-based Ni-pulldown assay that was successfully used in previous studies (24, 26). Interfacial residues in SHLD3 or REV7 were mutated into alanine, and the amount of SHLD3 peptide co-purifying with immobilized His-tagged REV7 was

evaluated and quantified. As expected, single alanine substitutions of REV7 Tyr-63 and Trp-171 showed dramatically reduced binding between REV7 and SHLD3, with relative band intensities being ~67.8 and 65.5% of the control level, respectively (Fig. 2*b*), whereas alanine substitution of Phe-169 had no significant effect on binding (Fig. 2*b*), suggesting that it makes a minor contribution to the SHLD3–REV7 interaction, in contrast to the significant contribution of this residue in formation of the CAMP–REV7 complex (26). Similar results were also observed in single Y37A, H57A, and F146A REV7 mutants that displayed only small changes in band intensities (Fig. 2*b*). But double mutation of Tyr-37 and Phe-146 to alanine decreased the binding by 21.4% (Fig. 2*b*), underlining their synergistic effect on mediating hydrophobic interaction with Pro-57 and Pro-58 of SHLD3. Notably, simultaneous alanine substitutions of Tyr-63 and Trp-171 in REV7 brought the most remarkable effect, with SHLD3–REV7 binding sharply reduced to about 11.2% of the control level (Fig. 2*b*), further suggesting van der Waals interactions formed by the two aromatic residues are important for maintaining SHLD3–REV7 interaction.

As for SHLD3, we found that single alanine substitutions of Pro-53, Pro-57, or Pro-58 in RBM almost retain full-binding ability to REV7 as the WT protein (Fig. 2*c*), a result distinct from CAMP–REV7 interaction where a single mutation of Pro-341 (also in RBM) of CAMP strikingly hinders its binding to REV7 (26). P53A/P57A double mutant also had no significant impact on the interaction between REV7 and SHLD3 (Fig. 2*c*). However, severely diminished interaction was observed when both Pro-53 and Pro-58 were replaced by alanine, and the Pro-57/Pro-58 double mutant also impaired the binding of SHLD3 to REV7 to 66.1% of that WT level (Fig. 2*c*). These results revealed Pro-58 is the most important one among the three prolines of RBM, whereas Pro-53 and Pro-57 exhibit relatively less significance during SHLD3–REV7 interaction. Additionally, the P50A mutant showed no decrease in band intensities, indicative of a minor role it also plays in interaction. To cross-validate the effects of the N-terminal loop mutants on REV7 interaction, we also conducted ITC measurements to observe the change of their binding affinity to REV7. In agreement with those observations in pulldown assays, the P53A/P57A double point mutant only had a subtle effect on binding with a K_D of 80.0 ± 2.5 nM, and the P57A/P58A mutant moderately diminished the binding by about 20.3-fold, with a K_D of 280.1 ± 4.6 nM (Fig. 2*d*). Once more, the largest defect was generated by the integration of two alanines into Pro-53 and Pro-58, which displayed a substantially reduced binding affinity of 2.1 ± 0.1 μM, nearly a 152.2-fold decrease that of the WT protein (Fig. 2*d*).

To determine the effects of these mutations in human cells, the Myc-tagged full-length SHLD3 harboring these mutations was co-transfected with SFB-tagged REV7. Consistent with previous reports (15, 19) and our *in vitro* results, the SHLD3 P53A/P58A double mutant largely decreased its binding to REV7 (Fig. 2*e*). Moreover, we observed that SHLD3 P57A/P58A double mutant also dramatically impaired the SHLD3–REV7 interaction, whereas SHLD3 P53A/P57A double mutant did not notably affect its binding to REV7 (Fig. 2*e*). However, as shown in Fig. 2*f*, SHLD3 retained binding ability to SFB-tagged REV7 F169A/W171A but failed to pull down SFB-tagged REV7
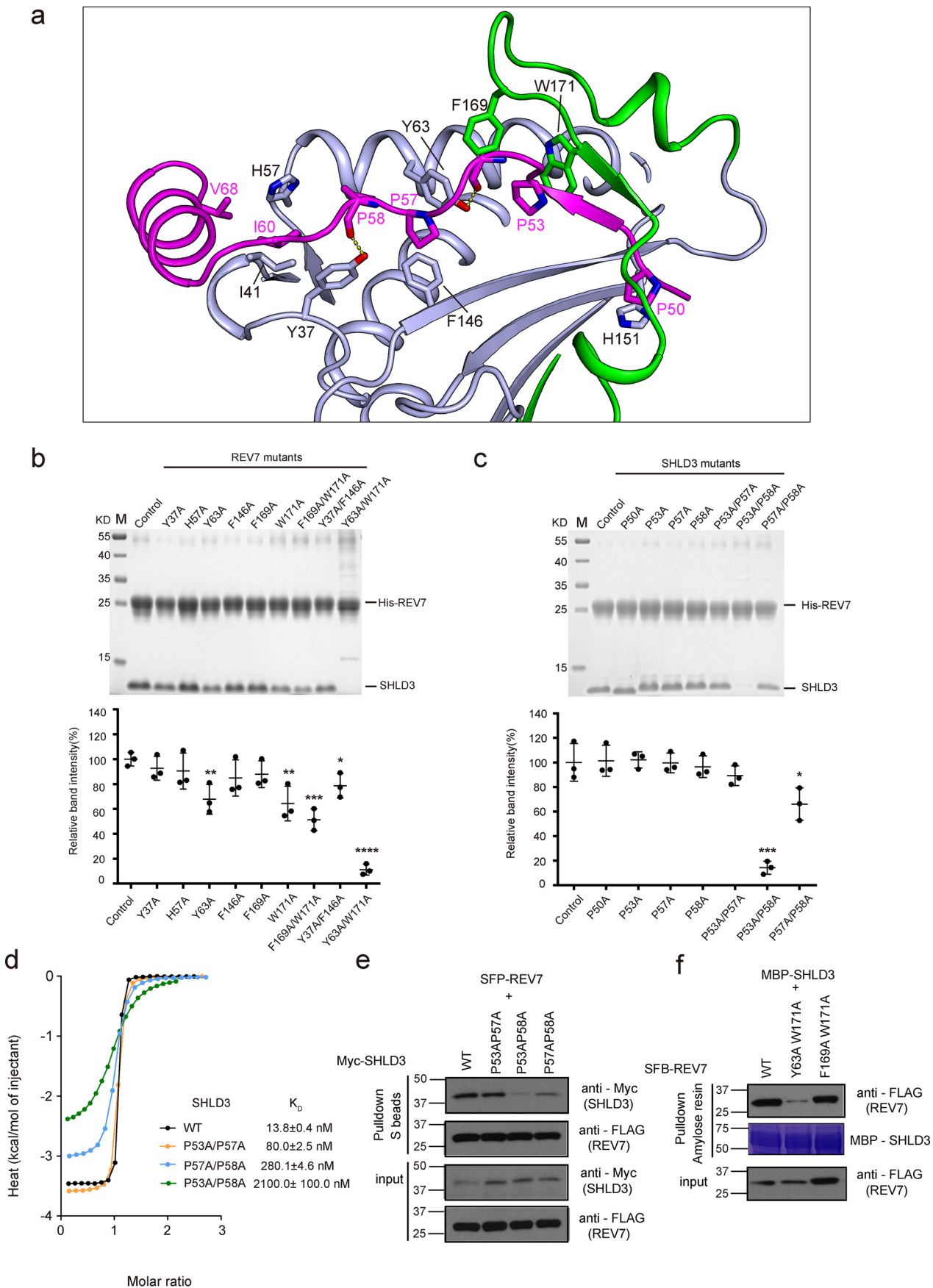
Y63A/W171A, indicating that the interaction between Tyr-63 and Pro-57/Pro-58 of SHLD3 plays a more vital role in SHLD3 binding *in vivo* than the interaction mediated by Trp-171 and Pro-53 of SHLD3. Collectively, these results corroborated that RBM in the N-terminal loop region of SHLD3–RBD is critical for REV7 binding.

αC-helix enables SHLD3's high-affinity recognition of REV7

Intriguingly, we observed the αC-helix of SHLD3–RBD interacts with REV7 through fitting into a shallow groove in the REV7 surface, acting as the base of the ladle configuration (Fig. 3*a*). This special conformation has not been observed in other known REV7-binding partners, as the "base" region of SHLD3–RBD points toward the backside of REV7 and forms a torsion angle of about 96.5°, whereas previous structures were either lacking the corresponding α-helix (CAMP) or adopting a relatively linear configuration (REV3–RBM1 and REV3–RBM2) (Fig. 3, *a* and *b*). Superimposition of the N-terminal loop region of SHLD3 RBD revealed the RMSD of 1.107 and 1.213 Å, although structural comparison of the full-length RBD from SHLD3 and from REV3–RBM1 or REV3–RBM2 leads to substantially increased RMSD for REV3–RBM1 (2.610 Å) and for REV3–RBM2 (2.649 Å), further suggesting conformational variations in the αC-helix region of SHLD3 RBD. Moreover, this unique conformation ensures a larger contact interface between SHLD3 and REV7, with an interacting area of 359.2 Å², as compared with the binding interface for REV3–RBM1 (166.5 Å²), REV3–RBM2 (241.7 Å²), and CAMP (78.3 Å²) (Fig. S4*a*).

It is conceivable that the larger interaction interface in this region contributes to stabilize and promote the binding between SHLD3 and REV7. Indeed, we observed that a SHLD3 fragment lacking the αC-helix region shows a remarkably reduced binding affinity in ITC assays, with a K_D of 505.1 ± 9.7 nM (Fig. 3*c*). Furthermore, the WT SHLD3 fragment interacts with REV7 in an enthalpically and entropically favorable manner, and the binding is mostly entropy-driven, but deletion of the αC-helix region largely compromised the favorable entropy (Fig. S4*b*), suggesting that the hydrophobic contacts conducted by this interface is crucial for the high-affinity SHLD3–REV7 interaction. A recent study reported that Ran also binds to REV7 via the classical RBM, but it is devoid of the corresponding SHLD3 αC-helix (30). The binding affinity between Ran and REV7 is about 900 nM, a level parallel to the SHLD3(Δ59–74) fragment (505.1 ± 9.7 nM) but considerably lower than WT peptide (13.8 ± 0.4 nM), which further accentuates the importance of SHLD3 αC-helix region in dictating high-affinity REV7 binding.

In this region of SHLD3, Ile-60 and Val-68 are two anchor residues as their hydrophobic side chains resemble a clamp that tightly holds the corresponding cavity in the REV7 surface (Fig. 2*a* and Fig. S4*a*). To dissect the roles of Ile-60 and Val-68 in mediating REV7 association, we made mutations to see whether the mutants displayed impaired binding. As shown in Fig. 3*c*, I60A mutation had an effect on SHLD3–REV7 interaction, reducing the binding to ~74.3% of the WT level. Furthermore, substitution of Ile-60 with an electrostatic residue remarkably impaired the binding to REV7, with I60K and I60D mutants displaying band intensities of 40.6 and 51.1% that of WT SHLD3 (Fig. 3*d*). Even though the I60A mutant did not display an obvious binding defect *in vivo*, SFB-tagged SHLD3 I60K indeed exhibited an impaired binding to REV7, and the SHLD3 P53A/I60K dual mutant showed a severely reduced capability to pull down REV7 (Fig. 3*e*). In addition, the I60K mutant also exhibited impaired binding affinity (K_D of 236.9 ± 10.5 nM) and decreased favorable entropy in ITC assays (Fig. 3*c*, Fig. S4*b*). These results validated the critical role of Ile-60 in maintaining SHLD3–REV7 cross-talk both *in vitro* and *in vivo*. It should be reminded that the SHLD3 Ile-60 is highly conserved in vertebrates (Fig. S1), implying this hydrophobic interaction is conserved and important in those species, too.

Moreover, the V68D mutant displayed an even weaker binding affinity (781.3 ± 9.2 nM) when compared with the I60K mutant (Fig. 3*c*), and the favorable entropy was also largely compromised (Fig. 4*b*).

The contribution of these two anchor residues is further affirmed by the Ni-pulldown assay using corresponding REV7 mutants. As shown in Fig. 3*f*, the dual mutation Y37S/H57A had no prominent effect on SHLD3–REV7 binding, as did the aforementioned H57A mutant. However, integration of Y37S/H57A with an extra I41D mutation markedly diminished the binding of SHLD3 to REV7 to ~28.9% that of the WT level, again demonstrating the hydrophobic interactions mediated by Ile-60 and Val-68 of SHLD3 are central to the high-affinity association between SHLD3 and REV7. Together, these results suggested that the αC-helix region of SHLD3–RBD underlies robust REV7 binding.

Safety-belt region promotes SHLD3–REV7 binding by retarding dissociation process

Like other RBM-containing protein, SHLD3 is also entangled with REV7 through a well-established "safety-belt" mode, but little is known about the mechanism of this intriguing process. To get better insights into the binding mechanism underlying the SHLD3–REV7 complex, we used SPR assays to study the

Figure 2. Structural basis of SHLD3(RBD)–REV7 complex. *a*, stereo view of the interaction details between SHLD3 and REV7. Colors of molecules correspond to those in Fig. 1*c*, and residues involved in the interaction are labeled. The hydrogen bonds are shown as *yellow dotted line*. *b* and *c*, Ni pulldown assays using His–REV7 co-expressed with SHLD3(29–83) fragments. After rounds of extensive washing, the bound proteins were resolved by SDS-PAGE stained with Coomassie Brilliant Blue (*upper panel*). His–REV7(R124A) was used as control sample. The *bottom plot panel* shows the relative abundance of the pulled down SHLD3 proteins. The relative band intensities of SHLD3(29–83) divided by band intensities of REV7 were normalized to those of the control. Values are represented as means ± S.D. from three independent experiments. One-tailed Student's tests are indicated: *, $p < 0.05$; **, $p < 0.01$; ***, $p < 0.001$; and ****, $p < 0.0001$. *d*, representative ITC results of the interactions between SHLD3 RBM mutants and REV7. Representative binding curves for WT, P53A/P57A, P53A/P58A, and P57A/P58A SHLD3 are shown as *black circle*, *yellow circle*, *green circle*, and *blue circle*, respectively. The binding affinity of each mutant is shown accordingly. *e*, 293T cells were transfected with plasmids encoding Myc-tagged SHLD3 WT and its mutants together with the plasmid encoding SFB-tagged REV7. Immunoprecipitation reactions were conducted using S protein beads and then subjected to Western blotting using the indicated antibodies. *f*, beads coated with bacterially expressed MBP-fused SHLD3 was incubated with cell lysates containing exogenously expressed SFB-tagged REV7 WT and its mutants. Immunoblotting experiments were carried out using the indicated antibodies.
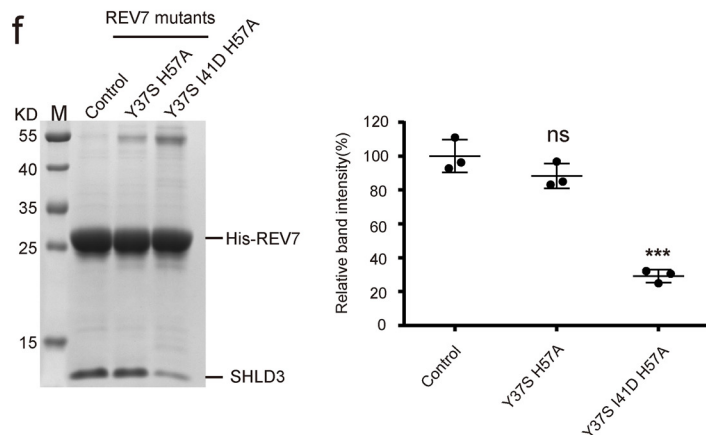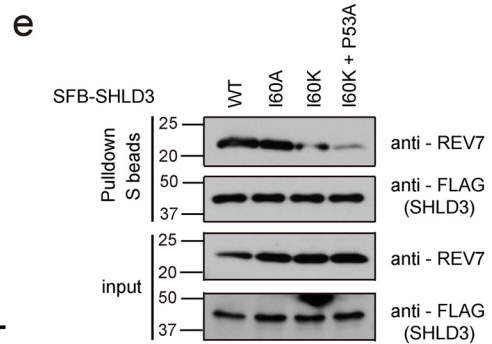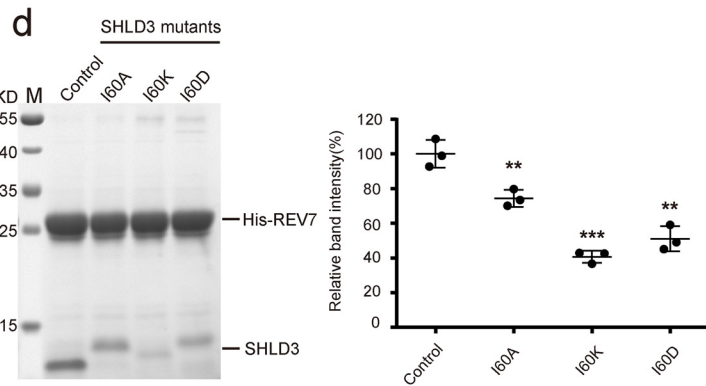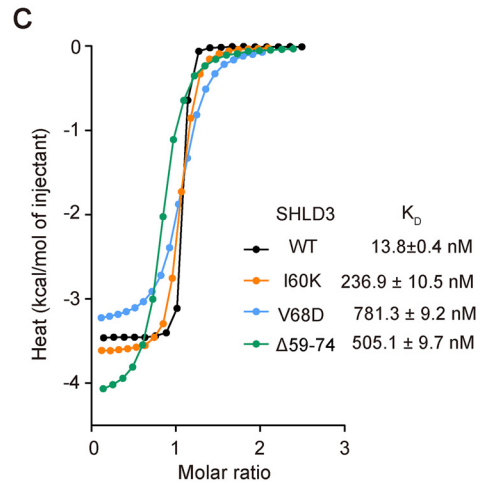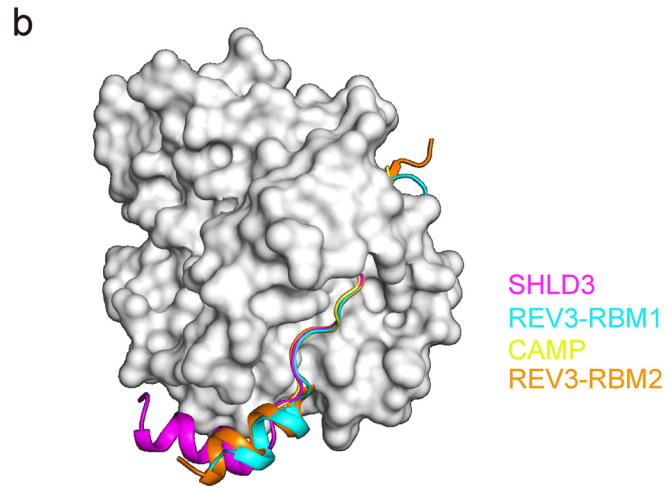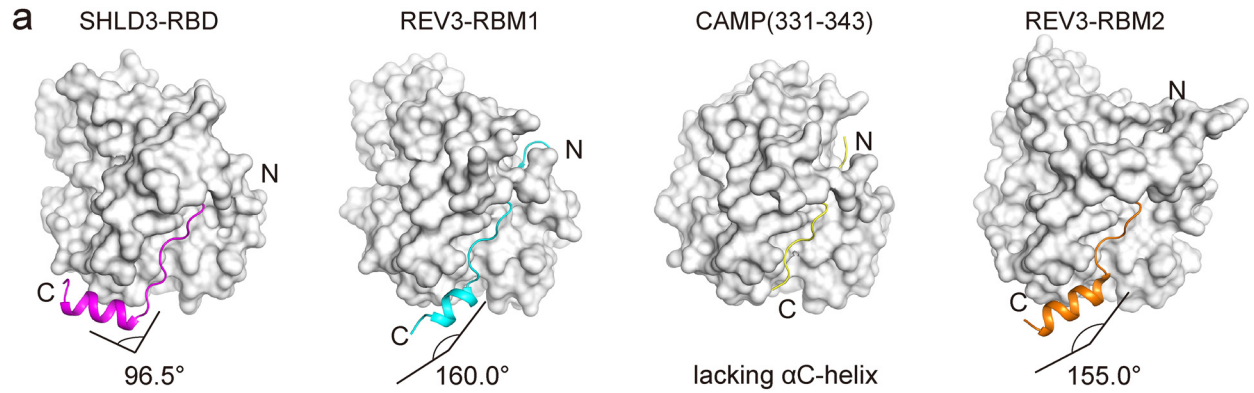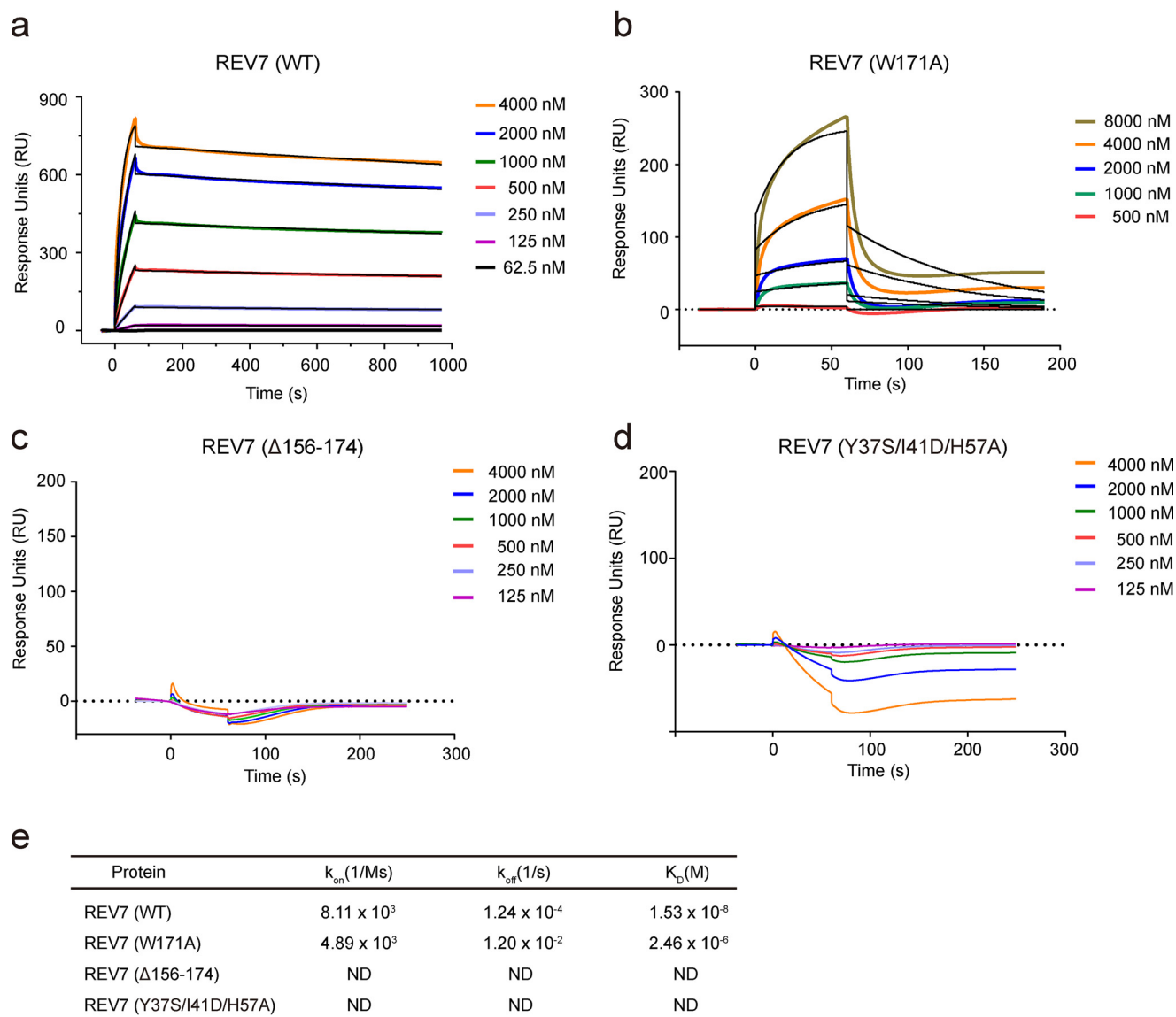
Figure 4. Binding kinetics of SHLD3–REV7 complex. *a–d*, SPR sensograms obtained during and after injection of MBP–REV7 or corresponding mutants over the immobilized SHLD3 chip surface. The model-fitting curve is displayed as *black lines* that overlay to the original sensograms. The concentrations of the MBP–REV7 proteins are indicated. *e*, statistics of association rate constant (k_{on}), dissociation rate constant (k_{off}), and equilibrium dissociation constant (K_D) of each reaction calculated from sensograms.

binding kinetics of this interaction. Purified SHLD3(29–83) fragment was immobilized onto a CM5 sensor, and 2-fold increasing concentrations of purified MBP–REV7 or mutants were injected and analyzed. As presented in Fig. 4*a*, the association rate constant (k_{on}) and the dissociation rate constant (k_{off}) of REV7 WT are 8.11×10^3 1/ms and 1.24×10^{-4} 1/s, respec-

tively. These rate constants generate a calculated equilibrium dissociation constant (K_D) of 15.3 nM (Fig. 4*e*), a number highly consistent with the ITC result (13.8 ± 0.4 nM) described above, confirming that the interaction between SHLD3 and REV7 has a K_D value in the low nanomolar, tight-binding range. Importantly, the safety-belt mutant W171A displayed an ~100-fold

Figure 3. αC-helix region of SHLD3–RBD underpins REV7–SHLD3 interaction. *a*, structural comparison of SHLD3 with other REV7-binding peptides. All REV7-binding segments are displayed in *cartoon* mode, and REV7 molecules are represented in surface mode. The angles between helix and loop of individual peptides are indicated. *Left to right:* SHLD3 (this study); REV3–RBM1 (PDB code 3ABD); CAMP (PDB code 5XPT); and REV3–RBM2 (PDB code 6BC8). *b*, structural superimposition of four REV7-binding partners. The REV7 molecule is represented in surface mode, and four fragments are shown in *cartoon* mode, with colors corresponding to those in *a*. *c*, representative ITC results of the interactions between SHLD3 mutants and REV7. The binding affinity and corresponding fitting curves are presented. Corresponding thermodynamic parameters are shown in Fig. S4b. *d*, Ni pulldown assays using His–REV7 co-expressed with Ile-60 mutants of SHLD3. The procedures are the same as depicted in Fig. 2 and under "Experimental procedures." The results of SDS-PAGE are shown in the *left panel*, and the *right scatter plot* shows the relative abundance of the pulled down SHLD3 proteins. Data are represented as means ± S.D. from three independent experiments. One-tailed Student's tests are indicated: **, $p < 0.01$; ***, $p < 0.001$. *e*, 293T cells were transfected with plasmids encoding SFB-tagged SHLD3 WT and its mutants. Immunoprecipitation reactions were conducted using S protein beads and then subjected to Western blotting using the indicated antibodies. *f*, Ni pulldown assays using His–REV7 mutants co-expressed with SHLD3(29–83) fragments. The procedures are the same as described above. The results of SDS-PAGE are shown in the *left panel*, and the *right scatter plot* shows the relative abundance of the pulled down SHLD3 proteins. Data are represented as means ± S.D. from three independent experiments. One-tailed Student's tests are indicated: *ns*, not significant; ***, $p < 0.001$.

higher dissociation rate constant of 1.20×10^{-2} 1/s and a 1.65-fold lower association rate constant of 4.89×10^3 1/ms in contrast to WT protein (Fig. 4, *b* and *e*). As a result, the calculated K_D of the W171A mutant is 2.46 μM, and this binding affinity is in accordance with the binding defect observed in *in vitro* Ni-pulldown assays (Fig. 2*b*). The prominent difference in dissociation rate manifested that the Trp-171 in the adaptor region of REV7 serves as a contributing factor of the tight-binding nature of the SHLD3–REV7 interaction by slowing down the dissociation process between REV7 and its cargoes. Moreover, we did not observe the interaction between an adaptor region deletion mutant (Δ156–174) and SHLD3 (Fig. 4, *c* and *e*), further suggesting this safety-belt loop contributes to REV7's interaction with its partners. Notably, REV7 Y37S/I41D/H57A mutant also showed an undetected binding to the SHLD3 peptide (Fig. 4, *d* and *e*), underscoring the contribution of interactions mediated by these residues and the αC-helix region of SHLD3 to complex formation.

Discussion

Recently, several contemporary reports exhaustively described the discovery of a four-subunit complex, termed Shieldin, working as the downstream effector of 53BP1–RIF1 to directly bind ssDNA and recruit CTC1-STN1-TEN1–polymerase α complex at damage sites that directs 3′ to 5′ fill-in DNA synthesis in opposition of the action of those end-processing nucleases (15–21, 31, 32). Among the four Shieldin subunits, SHLD3 is the most apical component that bridges REV7 to RIF1 and is crucial for correct localization of Shieldin at damage sites (16, 19, 22). Therefore, SHLD3–REV7 is considered as the DSB recruitment module within the Shieldin complex.

In this report, we determined the complex structure of SHLD3–RBD and REV7, where SHLD3–RBD adopts an unexpected ladle configuration to recognize REV7. Elegant studies by Gupta *et al.* (19) and Ghezraoui *et al.* (15) have shown that SHLD3–REV7 interaction relies predominantly on Pro-53 and Pro-58 in RBM, using either the immunofluorescence assay or the yeast two-hybrid system. Here, our findings provide the first structural evidence to explain their *in vivo* results, and they substantiate the RBM in the N-terminal loop of SHLD3 is required for REV7 binding. Meanwhile, the αC-helix region of SHLD3–RBD underpins the high-affinity interaction, as a SHLD3 fragment devoid of this part displayed largely compromised binding affinity (Fig. 3*c*). We then found Ile-60 and Val-68 act as two anchors in the αC-helix region of SHLD3, and this binding pattern is important for high-affinity REV7 binding.

Interestingly, we noticed that the double-anchor binding pattern similar to SHLD3 is also presented in two REV3 fragments, whereas CAMP adopts the single-anchor binding model in which an equivalent valine fills the same hydrophobic pocket in REV7 as does Ile-60 of SHLD3 (Fig. S4*a*). As the contribution of the second hydrophobic anchor in SHLD3–RBD to REV7 binding is significant, it is reasonable to infer that the binding affinity between REV3 and REV7 is comparable with SHLD3, and the interaction between CAMP and REV7 is much weaker due to the lack of corresponding structural elements. Of note, Ran interacts with REV7 via its RBM and exhibits a moderate binding affinity of about 900 nM (30), which parallels the binding affinity between REV7 and SHLD3 N-terminal loop containing RBM but is much lower than intact SHLD3–RBD. Therefore, the presence of an extra binding part in those proteins strikingly enhances their interaction with REV7. The variance in binding affinity, we surmise, is correlated with different biological functions. For example, during cell-cycle control and mitosis, REV7-binding partners are supposed to interact with REV7 at a given moment, and moderate binding affinity enables timely assembly/disassembly process between them and REV7. In addition, an ample amount of these proteins, such as Ran, makes it less necessary to possess tight binding. However, the abundance of SHLD3 in cells is ultra-low (undetectable in mass spectrometry–based global proteome analyses to a depth of ~10,000 proteins) (19). When DSB arises, the robust binding level ensures the recruitment of SHLD3 to REV7 and thus the proper repair of DNA damages.

Besides its role in DSB repair, the versatile REV7 protein also participates in other cellular pathways, such as TLS and cell-cycle control. The safety-belt region of REV7 plays a central role in various binding partners through an intriguing "open/close" switch, but lack of kinetic information impedes further understanding toward this process. Here, using SPR assays, we found the "safety belt" serves as a contributing factor of the tight-binding nature underlying the SHLD3–REV7 interaction by retarding the dissociation rate (Fig. 4*a*) because the mutation in safety-belt region impairs interaction mainly via drastically increasing the dissociation process (Fig. 4*b*). Additionally, we indeed observed the W171A mutant showed SHLD3-binding defects both in SPR assays using purified proteins and Ni-pulldown assays (Figs. 2*b* and 4*b*), but the W171A mutant did not have a detectable effect on SHLD3 binding *in vivo* (Fig. 2*f*) (15). This scientific disagreement could be explained by the possibility that other regulating factors in the complicated cell environment may modulate the safety-belt region of REV7 and affect its function during DSB repair. The potential regulators and mechanisms will be defined in a future study.

The safety belts are typical structural features among HORMA family proteins, which have structural plasticity and could be tuned between the open and closed state when interacting with different partners. In our structure, SHLD3 RBD is tightly locked by the safety belt of REV7, and this interaction, in turn, stabilizes the closed conformation of this region. But how REV7 dissociates from SHLD3 remains an open question, and other unknown factors or post-translational modifications, we speculate, may be involved in this process, as the safety belt of Mad2, the REV7 paralog, can be remodeled by ATPase TRIP13 to change from a closed conformation to the open conformation, thereby regulating the binding of Mad2 to its partners (33–35). Thus, future efforts are required to identify the regulator of SHLD3–REV7 dissociation and the corresponding molecular mechanism.

Recently, a structure-based screening has identified a potent small molecule that specifically targets the REV1 subunit within the mutagenic TLS complex, thus enhancing cisplatin-induced toxicity in human cell lines and restricting the growth of xenograft human melanomas in mice (36). REV7 is not only a component of the TLS complex but also a pivot in Shieldin complex,

and the SHLD3–REV7 structure exhibited some shallow grooves or cavities on REV7 surface suitable for various binding partners. Those are highly attractive sites for designing therapeutic inhibitors specific for blocking SHLD3–REV7 interaction. Importantly, it will provide feasible treatment strategies for those BRCA1-deficient patients that have developed resistance to the poly(ADP-ribose) polymerase inhibition remedy, as cells harboring defected Shieldin and BRCA1 mutants are more sensitive to ionizing radiation and cisplatin treatment (16, 17). Together, our work elucidated the molecular basis of the SHLD3–REV7 interaction and paved the way for the development of medicines toward cancer treatments.

Experimental procedures

Protein expression and purification

DNA sequences encoding human REV7(6–211) and SHLD3 fragments varying in length were amplified from human 293T cDNA and cloned into a pET-Duet-1 vector using BamHI/NotI and NdeI/XhoI sites, respectively, which generate the His-tag REV7 and nontag SHLD3 peptide. Mutations of R124A and/or A135D were introduced into REV7 to stabilize the protein (23–25), allowing subsequent crystal screen trials. For co-expression of various His–REV7(6–211)–SHLD3, the plasmids were transformed into *Escherichia coli* BL21-Codon PLUS(DE3)-RIPL cells. When the cells grown at 37 °C reached an OD_{600} of 0.8, 0.5 mM isopropyl β-D-thiogalactoside (IPTG) was added to the LB medium to induce protein expression at 16 °C for 18 h. Then, the cells were collected and lysed in buffer A (50 mM Hepes, pH 7.4, 500 mM NaCl, 20 mM imidazole). Supernatants separated by centrifugation were applied onto a self-packed Ni-NTA column (Qiagen) equilibrated with buffer A. After washing steps using buffer A and buffer B (20 mM Hepes, pH 7.4, 1.5 M NaCl), the targeted proteins were eluted with buffer C (20 mM Tris-HCl, pH 8.0, 100 mM NaCl, 300 mM imidazole), immediately diluted with buffer D (20 mM Tris-HCl, pH 8.0), and then loaded onto a 5-ml HiTrap Q HP column (GE Healthcare) for further purification. The bound proteins were eluted against a linear gradient from 50 to 800 mM NaCl. The eluate containing REV7–SHLD3 complexes was concentrated using 10,000 MWCO centrifugal filter units (Millipore) and subjected to size-exclusion chromatography (GE Healthcare) equilibrated with buffer E (20 mM Hepes, pH 7.4, 100 mM NaCl) for final purification. The purified protein complexes were fast-frozen in liquid nitrogen and stored at −80 °C until use.

For protein used in ITC assays, full-length REV7 was constructed into a homemade pET28a vector to have a His–MBP fusion tag at the N terminus, which greatly improved the solubility. To effectively avoid degradation and promote purification, SHLD3(29–83) fragment was cloned into another designed pET28a vector to make a recombinant SHLD3 fusion protein with a His-tag at the N terminus and a yeast Smt3 tag at the C terminus. Constructs were expressed in BL21–Codon PLUS(DE3)–RIPL cells, in LB medium induced with 0.4 mM IPTG for 18 h at 16 °C. The proteins were purified similarly as described above. The purified protein samples were concentrated and stored at −80 °C after flash-freezing in liquid nitrogen until use. Mutations were generated using the QuikChange

site-directed mutagenesis kit (Stratagene) and were verified by sequencing. Resulting protein mutants were purified in the same way as WT protein.

Crystallization, data collection, and structure determination

For crystallization attempts, REV7 complexed with SHLD3 segments of various lengths were used. The crystallization was performed by mixing 1.2-μl protein complexes (20 mg/ml) with a 1.2-μl reservoir solution using the hanging-drop vapor-diffusion method. Nearly 3 days later, crystals appeared at several conditions. After optimization of the reservoir conditions, crystals of good quality come from the REV7(R124A)–SHLD3(46–74) complex in a reservoir solution containing 0.1 M sodium acetate, pH 5.2, 2.1 M ammonium sulfate, and REV7(R124A/A135D)–SHLD3(46–74) complex in a reservoir solution consisted of 0.1 M sodium citrate tribasic, pH 5.0, 1.9 M ammonium sulfate. Then, each crystal was collected within a nylon loop and transferred to liquid nitrogen with cryoprotectant made from the corresponding reservoir solution plus 25% glycerol until use. Diffraction data were collected at the Shanghai Synchrotron Radiation Facility (SSRF) BL17U1 beamline using the Eiger X 16M detector or BL19U1 beamline using the PILATUS 6M detector. All collected data were processed and scaled using the XDS package (37) and AIMLESS (38) within the CCP4 program suite (39). As both crystals displayed anisotropy, the data were further corrected with UCLA diffraction anisotropy server (40), which improved the resulting electron density maps and enabled unambiguous model building.

For REV7(R124A)–SHLD3(46–74) complex, the structure was determined by the molecular replacement method using REV7–REV3 (PDB code 3ABD) as a template with the program PHASER (41). Manual model building and subsequent refinement were performed in program COOT (42) and program PHENIX (43), respectively. The final structure, refined to $R_{work}/R_{free} = 20.4/24.6\%$, contains REV7 residues 9–207 and SHLD3 residues 49–73. Residues without discernable side-chain density were truncated at the β-carbon. As validated by MolProbity (44), the final model showed good stereochemistry with 94.34% residues in the Ramachandran-favored region, 5.66% residues in Ramachandran-allowed zones, and no outliers. Other statistics during data collection and processing were summarized in Table 1.

For the REV7(R124A/A135D)–SHLD3(46–74) complex, the structure was determined in the same procedure as described for the REV7(R124A)–SHLD3(46–74) complex. The final structure, validated with MolProbity program, showed 96.82% favored, 3.18% allowed, and no outliers in the Ramachandran plot. Details of the structural statistics are shown in Table 1. All structural figures were prepared using the PyMOL program (The PyMOL Molecular Graphics System, Version 2.2.0 Schrödinger, LLC).

IMAC-based interaction assays

Mutations in REV7 or SHLD3 were introduced using the QuikChange site-directed mutagenesis kit (Stratagene) into a pET-Duet-1 vector, enabling co-expression of His–REV7 and SHLD3(29–83) peptides. Interaction analysis by IMAC was performed, as described previously (24, 26), with minor differ-

ences. Briefly, after cell lysis and centrifugation, the soluble fractions were incubated with Ni-NTA resins (Qiagen) at 4 °C for 2 h. The beads were first washed with buffer F (20 mM Hepes, pH 7.4, 1.5 M NaCl, 20 mM imidazole) three times and then washed using buffer B another three times. Next, the bound proteins were eluted with buffer C and analyzed by SDS-PAGE stained with Coomassie Brilliant Blue. Band intensities were quantified in program Quantity One (Bio-Rad). The quantification results came from three independent experiments, and the statistical significance of differences between samples was determined by an unpaired Student's *t* test, using GraphPad Prism 6 (GraphPad Software).

Isothermal titration calorimetry experiments

Purified proteins used here were dialyzed overnight against ITC buffer (20 mM Tris-HCl, pH 7.5, 150 mM NaCl, 2 mM β-mercaptoethanol), and all measurements were done using an ITC200 titration calorimeter (MicroCal) at 20 °C. A pre-drop of 0.4 μl and a subsequent 19 2.0-μl drops of His–SHLD3–Smt3 (300–500 μM) were stepwise-injected into the calorimetric cell containing His–MBP–REV7 (20–50 μM), at intervals of 120 s. The stirring speed remained constant at 750 rpm to thoroughly mix the samples in the cell. In all cases, two independent experiments were performed. As described previously (45), the raw data were analyzed and fitted into a one-site binding model using Origin 7.0 software (Microcal). The relationships between change in enthalpy (ΔH), entropy (ΔS), and binding energy (ΔG) were calculated as $\Delta G = \Delta H - T\Delta S$.

Surface plasmon resonance measurements

Binding kinetics assays were performed on a BIAcore 8K instrument (BIAcore AB, Uppsala, Sweden). Purified SHLD3(29–83) fragment was immobilized on a research-grade CM5 chip using EDC–NHS coupling chemistry according to the BIAcore manual, and 2-fold increasing concentrations of purified MBP–REV7 or mutants were injected and analyzed. The SPR running buffer is 20 mM Hepes-Na, pH 7.5, 150 mM NaCl, 0.05% v/v Tween 20, and analyses were recorded at 25 °C, whereas a 20 mM NaOH buffer was used as regeneration buffer. All of the data collected were analyzed in BIAevaluation software (BIAcore). The association (k_{on}) and dissociation (k_{off}) rates and the equilibrium dissociation constant (K_D) were obtained using a 1:1 Langmuir binding model.

Co-immunoprecipitation and Western blotting

Cells were lysed with NTEN buffer (20 mM Tris-HCl, pH 8.0, 100 mM NaCl, 1 mM EDTA, 0.5% Nonidet P-40) containing pepstatin A and aprotinin on ice for 30 min. Clear cell lysates were incubated with S protein beads for 2 h at 4 °C. Beads were then washed and boiled in 2× Laemmli buffer, and proteins were separated by SDS-PAGE. Polyvinylidene difluoride membranes were blocked in 5% milk in TBST buffer and then probed with antibodies as indicated.

Data availability

Atomic coordinates and structure factors for the REV7 (R124A)–SHLD3 and REV7(R124A/A135D)–SHLD3 complexes have been deposited to the Protein Data Bank under accession numbers 6K07 and 6K08, respectively.

References

1. Heyer, W.-D., Ehmsen, K. T., and Liu, J. (2010) Regulation of homologous recombination in Eukaryotes. *Annu. Rev. Genet.* **44,** 113–139 CrossRef Medline
2. Lieber, M. R. (2010) The mechanism of double-strand DNA break repair by the nonhomologous DNA end-joining pathway. *Annu. Rev. Biochem.* **79,** 181–211 CrossRef Medline
3. Chapman, J. R., Taylor, M. R., and Boulton, S. J. (2012) Playing the end game: DNA double-strand break repair pathway choice. *Mol. Cell* **47,** 497–510 CrossRef Medline
4. Panier, S., and Boulton, S. J. (2014) Double-strand break repair: 53BP1 comes into focus. *Nat. Rev. Mol. Cell Biol.* **15,** 7–18 CrossRef Medline
5. Bunting, S. F., Callén, E., Wong, N., Chen, H.-T., Polato, F., Gunn, A., Bothmer, A., Feldhahn, N., Fernandez-Capetillo, O., Cao, L., Xu, X., Deng, C.-X., Finkel, T., Nussenzweig, M., Stark, J. M., and Nussenzweig, A. (2010) 53BP1 Inhibits homologous recombination in Brca1-deficient cells by blocking resection of DNA breaks. *Cell* **141,** 243–254 CrossRef Medline
6. Bouwman, P., Aly, A., Escandell, J. M., Pieterse, M., Bartkova, J., van der Gulden, H., Hiddingh, S., Thanasoula, M., Kulkarni, A., Yang, Q., Haffty, B. G., Tommiska, J., Blomqvist, C., Drapkin, R., Adams, D. J., *et al.* (2010) 53BP1 loss rescues BRCA1 deficiency and is associated with triple-negative and BRCA-mutated breast cancers. *Nat. Struct. Mol. Biol.* **17,** 688–695 CrossRef Medline
7. Di Virgilio, M., Callen, E., Yamane, A., Zhang, W., Jankovic, M., Gitlin, A. D., Feldhahn, N., Resch, W., Oliveira, T. Y., Chait, B. T., Nussenzweig, A., Casellas, R., Robbiani, D. F., and Nussenzweig, M. C. (2013) Rif1 prevents resection of DNA breaks and promotes immunoglobulin class switching. *Science* **339,** 711–715 CrossRef Medline
8. Chapman, J. R., Barral, P., Vannier, J.-B., Borel, V., Steger, M., Tomas-Loba, A., Sartori, A. A., Adams, I. R., Batista, F. D., and Boulton, S. J. (2013) RIF1 is essential for 53BP1-dependent nonhomologous end joining and suppression of DNA double-strand break resection. *Mol. Cell* **49,** 858–871 CrossRef Medline
9. Escribano-Díaz, C., Orthwein, A., Fradet-Turcotte, A., Xing, M., Young, J. T., Tkáč, J., Cook, M. A., Rosebrock, A. P., Munro, M., Canny, M. D., Xu, D., and Durocher, D. (2013) A cell cycle-dependent regulatory circuit composed of 53BP1–RIF1 and BRCA1-CtIP controls DNA repair pathway choice. *Mol. Cell* **49,** 872–883 CrossRef Medline
10. Feng, L., Fong, K.-W., Wang, J., Wang, W., and Chen, J. (2013) RIF1 counteracts BRCA1-mediated end resection during DNA repair. *J. Biol. Chem.* **288,** 11135–11143 CrossRef Medline
11. Boersma, V., Moatti, N., Segura-Bayona, S., Peuscher, M. H., van der Torre, J., Wevers, B. A., Orthwein, A., Durocher, D., and Jacobs, J. J. (2015)

MAD2L2 controls DNA repair at telomeres and DNA breaks by inhibiting 5′ end resection. *Nature* **521,** 537–540 CrossRef Medline

12. Xu, G., Chapman, J. R., Brandsma, I., Yuan, J., Mistrik, M., Bouwman, P., Bartkova, J., Gogola, E., Warmerdam, D., Barazas, M., Jaspers, J. E., Watanabe, K., Pieterse, M., Kersbergen, A., Sol, W., *et al.* (2015) REV7 counteracts DNA double-strand break resection and affects PARP inhibition. *Nature* **521,** 541–544 CrossRef Medline

13. Drané, P., Brault, M.-E., Cui, G., Meghani, K., Chaubey, S., Detappe, A., Parnandi, N., He, Y., Zheng, X.-F., Botuyan, M. V., Kalousi, A., Yewdell, W. T., Münch, C., Harper, J. W., Chaudhuri, J., *et al.* (2017) TIRR regulates 53BP1 by masking its histone methyl-lysine binding function. *Nature* **543,** 211–216 CrossRef Medline

14. Zhang, A., Peng, B., Huang, P., Chen, J., and Gong, Z. (2017) The p53-binding protein 1-Tudor-interacting repair regulator complex participates in the DNA damage response. *J. Biol. Chem.* **292,** 6461–6467 CrossRef Medline

15. Ghezraoui, H., Oliveira, C., Becker, J. R., Bilham, K., Moralli, D., Anzilotti, C., Fischer, R., Deobagkar-Lele, M., Sanchiz-Calvo, M., Fueyo-Marcos, E., Bonham, S., Kessler, B. M., Rottenberg, S., Cornall, R. J., Green, C. M., and Chapman, J. R. (2018) 53BP1 cooperation with the REV7–shieldin complex underpins DNA structure-specific NHEJ. *Nature* **560,** 122–127 CrossRef Medline

16. Noordermeer, S. M., Adam, S., Setiaputra, D., Barazas, M., Pettitt, S. J., Ling, A. K., Olivieri, M., Álvarez-Quilón, A., Moatti, N., Zimmermann, M., Annunziato, S., Krastev, D. B., Song, F., Brandsma, I., Frankum, J., *et al.* (2018) The shieldin complex mediates 53BP1-dependent DNA repair. *Nature* **560,** 117–121 CrossRef Medline

17. Dev, H., Chiang, T.-W., Lescale, C., de Krijger, I., Martin, A. G., Pilger, D., Coates, J., Sczaniecka-Clift, M., Wei, W., Ostermaier, M., Herzog, M., Lam, J., Shea, A., Demir, M., Wu, Q., *et al.* (2018) Shieldin complex promotes DNA end-joining and counters homologous recombination in BRCA1-null cells. *Nat. Cell Biol.* **20,** 954–965 CrossRef Medline

18. Gao, S., Feng, S., Ning, S., Liu, J., Zhao, H., Xu, Y., Shang, J., Li, K., Li, Q., Guo, R., and Xu, D. (2018) An OB-fold complex controls the repair pathways for DNA double-strand breaks. *Nat. Commun.* **9,** 3925 CrossRef Medline

19. Gupta, R., Somyajit, K., Narita, T., Maskey, E., Stanlie, A., Kremer, M., Typas, D., Lammers, M., Mailand, N., Nussenzweig, A., Lukas, J., and Choudhary, C. (2018) DNA repair network analysis reveals Shieldin as a key regulator of NHEJ and PARP inhibitor sensitivity. *Cell* **173,** 972–988.e23 CrossRef Medline

20. Findlay, S., Heath, J., Luo, V. M., Malina, A., Morin, T., Coulombe, Y., Djerir, B., Li, Z., Samiei, A., Simo-Cheyou, E., Karam, M., Bagci, H., Rahat, D., Grapton, D., Lavoie, E. G., *et al.* (2018) SHLD2/FAM35A co-operates with REV7 to coordinate DNA double-strand break repair pathway choice. *EMBO J.* **37,** e100158 CrossRef Medline

21. Tomida, J., Takata, K. I., Bhetawal, S., Person, M. D., Chao, H. P., Tang, D. G., and Wood, R. D. (2018) FAM35A associates with REV7 and modulates DNA damage responses of normal and BRCA1-defective cells. *EMBO J.* **37,** e99543 CrossRef Medline

22. Setiaputra, D., and Durocher, D. (2019) Shieldin–the protector of DNA ends. *EMBO Rep.* **20,** e47560 CrossRef Medline

23. Hara, K., Shimizu, T., Unzai, S., Akashi, S., Sato, M., and Hashimoto, H. (2009) Purification, crystallization and initial X-ray diffraction study of human REV7 in complex with a REV3 fragment. *Acta Crystallogr. Sect. F Struct. Biol. Cryst. Commun.* **65,** 1302–1305 CrossRef Medline

24. Hara, K., Hashimoto, H., Murakumo, Y., Kobayashi, S., Kogame, T., Unzai, S., Akashi, S., Takeda, S., Shimizu, T., and Sato, M. (2010) Crystal structure of human REV7 in complex with a human REV3 fragment and structural implication of the interaction between DNA polymerase ζ and REV1. *J. Biol. Chem.* **285,** 12299–12307 CrossRef Medline

25. Rizzo, A. A., Vassel, F.-M., Chatterjee, N., D'Souza, S., Li, Y., Hao, B., Hemann, M. T., Walker, G. C., and Korzhnev, D. M. (2018) Rev7 dimerization is important for assembly and function of the Rev1/Polζ translesion synthesis complex. *Proc. Natl. Acad. Sci. U.S.A.* 115, E8191–E8200 CrossRef Medline

26. Hara, K., Taharazako, S., Ikeda, M., Fujita, H., Mikami, Y., Kikuchi, S., Hishiki, A., Yokoyama, H., Ishikawa, Y., Kanno, S. I., Tanaka, K., and

27. Hashimoto, H. (2017) Dynamic feature of mitotic arrest deficient 2–like protein 2 (MAD2L2) and structural basis for its interaction with chromosome alignment–maintaining phosphoprotein (CAMP). *J. Biol. Chem.* **292,** 17658–17667 CrossRef Medline

27. Kikuchi, S., Hara, K., Shimizu, T., Sato, M., and Hashimoto, H. (2012) Structural basis of recruitment of DNA polymerase ζ by interaction between REV1 and REV7 proteins. *J. Biol. Chem.* **287,** 33847–33852 CrossRef Medline

28. Wojtaszek, J., Lee, C.-J., D'Souza, S., Minesinger, B., Kim, H., D'Andrea, A. D., Walker, G. C., and Zhou, P. (2012) Structural basis of Rev1-mediated assembly of a quaternary vertebrate translesion polymerase complex consisting of Rev1, heterodimeric polymerase (Pol) ζ, and Pol κ. *J. Biol. Chem.* **287,** 33836–33846 CrossRef Medline

29. Xie, W., Yang, X., Xu, M., and Jiang, T. (2012) Structural insights into the assembly of human translesion polymerase complexes. *Protein Cell* **3,** 864–874 CrossRef Medline

30. Wang, X., Pernicone, N., Pertz, L., Hua, D., Zhang, T., Listovsky, T., and Xie, W. (2019) REV7 has a dynamic adaptor region to accommodate small GTPase RAN/*Shigella* IpaB ligands and its activity is regulated by RanGTP/GDP switch. *J. Biol. Chem.* 294, 15733–15742 CrossRef Medline

31. Mirman, Z., Lottersberger, F., Takai, H., Kibe, T., Gong, Y., Takai, K., Bianchi, A., Zimmermann, M., Durocher, D., and de Lange, T. (2018) 53BP1–RIF1–shieldin counteracts DSB resection through CST- and Polα-dependent fill-in. *Nature* **560,** 112–116 CrossRef Medline

32. Barazas, M., Annunziato, S., Pettitt, S. J., de Krijger, I., Ghezraoui, H., Roobol, S. J., Lutz, C., Frankum, J., Song, F. F., Brough, R., Evers, B., Gogola, E., Bhin, J., van de Ven, M., van Gent, D. C., Jacobs, J. J. L., *et al.* (2018) The CST complex mediates end protection at double-strand breaks and promotes PARP inhibitor sensitivity in BRCA1-deficient cells. *Cell Rep.* **23,** 2107–2118 CrossRef Medline

33. Ye, Q., Rosenberg, S. C., Moeller, A., Speir, J. A., Su, T. Y., and Corbett, K. D. (2015) TRIP13 is a protein-remodeling AAA⁺ ATPase that catalyzes MAD2 conformation switching. *Elife* **4,** 10.7554/eLife.07367 Medline

34. Alfieri, C., Chang, L., and Barford, D. (2018) Mechanism for remodelling of the cell cycle checkpoint protein MAD2 by the ATPase TRIP13. *Nature* **559,** 274–278 CrossRef Medline

35. Brulotte, M. L., Jeong, B.-C., Li, F., Li, B., Yu, E. B., Wu, Q., Brautigam, C. A., Yu, H., and Luo, X. (2017) Mechanistic insight into TRIP13-catalyzed Mad2 structural transition and spindle checkpoint silencing. *Nat. Commun.* **8,** 1956 CrossRef Medline

36. Wojtaszek, J. L., Chatterjee, N., Najeeb, J., Ramos, A., Lee, M., Bian, K., Xue, J. Y., Fenton, B. A., Park, H., Li, D., Hemann, M. T., Hong, J., Walker, G. C., and Zhou, P. (2019) A small molecule targeting mutagenic translesion synthesis improves chemotherapy. *Cell* **178,** 152–159.e11 CrossRef Medline

37. Kabsch, W. (2010) XDS. *Acta Crystallogr. D Biol. Crystallogr.* **66,** 125–132 CrossRef Medline

38. Evans, P. R., and Murshudov, G. N. (2013) How good are my data and what is the resolution? *Acta Crystallogr. D Biol. Crystallogr.* **69,** 1204–1214 CrossRef Medline

39. Winn, M. D., Ballard, C. C., Cowtan, K. D., Dodson, E. J., Emsley, P., Evans, P. R., Keegan, R. M., Krissinel, E. B., Leslie, A. G., McCoy, A., McNicholas, S. J., Murshudov, G. N., Pannu, N. S., Potterton, E. A., Powell, H. R., *et al.* (2011) Overview of the CCP4 suite and current developments. *Acta Crystallogr. D Biol. Crystallogr.* **67,** 235–242 CrossRef Medline

40. Strong, M., Sawaya, M. R., Wang, S., Phillips, M., Cascio, D., and Eisenberg, D. (2006) Toward the structural genomics of complexes: crystal structure of a PE/PPE protein complex from *Mycobacterium tuberculosis*. *Proc. Natl. Acad. Sci. U.S.A.* **103,** 8060–8065 CrossRef Medline

41. McCoy, A. J., Grosse-Kunstleve, R. W., Adams, P. D., Winn, M. D., Storoni, L. C., and Read, R. J. (2007) Phaser crystallographic software. *J. Appl. Crystallogr.* **40,** 658–674 CrossRef Medline

42. Emsley, P., and Cowtan, K. (2004) Coot: model-building tools for molecular graphics. *Acta Crystallogr. D Biol. Crystallogr.* **60,** 2126–2132 CrossRef Medline

43. Adams, P. D., Afonine, P. V., Bunkóczi, G., Chen, V. B., Davis, I. W., Echols, N., Headd, J. J., Hung, L.-W., Kapral, G. J., Grosse-Kunstleve, R. W., Mc-

Coy, A. J., Moriarty, N. W., Oeffner, R., Read, R. J., Richardson, D. C., *et al.* (2010) PHENIX: a comprehensive Python-based system for macromolecular structure solution. *Acta Crystallogr. D Biol. Crystallogr.* **66,** 213–221 CrossRef Medline

44. Chen, V. B., Arendall, W. B., 3rd., Headd, J. J., Keedy, D. A., Immormino, R. M., Kapral, G. J., Murray, L. W., Richardson, J. S., and Richardson, D. C. (2010) MolProbity: all-atom structure validation for macromolecular crystallography. *Acta Crystallogr. D Biol. Crystallogr.* **66,** 12–21 CrossRef Medline

45. Dai, Y., Zhang, A., Shan, S., Gong, Z., and Zhou, Z. (2018) Structural basis for recognition of 53BP1 tandem Tudor domain by TIRR. *Nat. Commun.* **9,** 2123 CrossRef Medline